Research Article

Active Vibration Control of a Large Flexible Appendage Using a Novel Joint Mechanism

Wei Hu [iD], Jianming Wu, Qinghua Zhu, Jie Shen, Xunjiang Zheng, Shaoyong Sun, Xiaonan Mao, Honglei Cao, and Yucong Tang

Shanghai Aerospace Control Technology Institute, Shanghai 201109, China

Correspondence should be addressed to Wei Hu; sjtuwhu@126.com

With the evolution of space exploration, large flexible appendages have been developed in space structures. External perturbation or attitude maneuvering stimulates the vibration (low frequencies) of the aforementioned structures. In this research, a novel joint mechanism was developed in conjunction with active control to inhibit the low-frequency vibration of a large flexible appendage. A compact active joint, based on the idea of electromagnetic direct drive, was designed. The dynamic equations for the large flexible appendage system and the active joint were derived using the Lagrange function with the assumed-modes approach. Single- and multi-frequency excitations were simulated by two noncontact strategies for periodic vibration stimulation along the direction of rotation. The research results revealed that the interference signal had a primary frequency bandwidth of 0.07–0.63 Hz, and the vibration attenuation was prominent between 5.95 and 32.41 dB within the valid bandwidth. Effective inhibition of both the larger and the smaller amplitude vibrations at frequencies lower than 1 Hz could be realized using the proposed active joint without attachment of intelligent materials onto the flexible appendage surface.

1. Introduction

Due to low damping, lightweight, long span, and low stiffness of space flexible structures, the structures inherently exhibit low-frequency nonlinear vibrations. Because temperature shocks or space particles affect the spacecraft during its entry/departure from the Earth shadow or during attitude maneuvering, the vibrations of flexible appendage inevitably exist in structural terms. Typically, the vibration frequencies of such large structures are lower than 1 Hz, and achieving natural damping in an elevated atmosphere and under micro-gravity conditions is difficult. The spacecraft pointing accuracy becomes compromised in case vibrations are not suppressed efficiently. Spacecraft is considerably affected by such low-frequency vibrations. Therefore, the investigation of low-frequency vibrations for flexible spacecraft is critical [1–6].

The following two major types of control strategies have been reported in literature: the passive control methods based on viscoelastic damping materials and the active control methods based on piezoelectric materials. The implementation of passive control is easy, and its structure is simple [7, 8]. Vibrations can be isolated through appropriate arrangement of damper materials at the appropriate positions of mechanisms/structures. However, passive control cannot satisfactorily suppress abrupt contextual changes, which are influenced by the weights of structure and materials. For various design conditions, passive vibration controllers can become ineffective rapidly. Active vibration isolation techniques differ considerably from passive techniques. In control and modeling literature, the flexible beams driven by motors [9–11] have been investigated broadly, and because of multipurpose use including accurate tracking control of the beam tip end-effector and suppression of related vibrations, vibration control becomes challenging [12–14]. As an intelligent material, piezoelectric is typically used for additional stiffening and damping activities to inhibit unwanted vibration. To improve control performance, numerous active control algorithms have been proposed (e.g., neural network control [15], sliding mode

control [16], fuzzy control [17–19], robust control [20, 21], adaptive control [22, 23], nonlinear control algorithm [17, 24], and data-driven control [25]). Despite excellent micro-amplitude drive, intelligent materials exhibit a few shortcomings related to large stroke drive and control [26–31].

Accordingly, in this study, a novel active joint mechanism is proposed to suppress both the larger and the smaller amplitude vibrations at low frequencies below 1 Hz just by active joint, without attachment of intelligent material onto the flexible appendage surface. The proposed joint mechanism shows a certain novelty for realizing compact structure, micro-amplitude drive, integration of structure and function, and real-time control. Our major innovations are as follows:

(a) *Electromagnetic Direct Drive.* The proposed joint mechanism, based upon the idea of direct driving, exhibits a compact construction and operates in conjunction with an electro-permanent-magnet driving mechanism. Because the spindle is directly linked to the load, the clearance and friction generated by intermediary transmission devices, such as gears and belts, are minimized.

(b) *Integration of Structural and Functional Characteristics.* The joint is placed between adjacent appendages, which simultaneously serve as a functional part and a structural connector. The joint mechanism performs as a structural element, establishing firm connections and supporting neighboring appendages. It also behaves as a functional portion, allowing appendages to deploy, retract, and vibrate.

(c) *Integration of Deployment/Retraction and Vibration Control.* The described joint system has the potential to be employed in flexible appendages, such as solar panels, to create appendages with self-deploying/folding functionalities and vibration control capacity.

When alternating current (AC) power is used, deployment and retraction can be actively conducted. The appendage can be spread freely with no impact, and particularly, they can be recycled. Each 60° rotational movement can be achieved using the driving unit with a single impulse-current excitation, thereby facilitating the control easier and making the power supply highly efficient. The panel can be directly driven to deploy/fold for 180° through only three impulse signals in the coils. Moreover, the damping effects can be naturally generated through attraction forces between the rotational permanent magnet and yoke. This damping provides protection from the overshooting of deploying/folding action or vibration.

When direct current (DC) power is supplied, the joint mechanism shows varying stiffness characteristics. When the external stimulation is near the system's resonance frequencies, the joint torsional stiffness can be altered by varying the electric current, resulting in the system's frequency-shift phenomenon. Consequently, the isolation effect can be

obtained. In addition, the active control algorithm is used to actively suppress the low-frequency vibration of the flexible appendage. When the appendage is subjected to periodic excitation disturbance, the joint provides the output torque of same frequency but in reverse direction to reduce the appendage vibration. The real-time angular displacement feedback is employed to control the input current. The output torque of the joint mechanism is proportional to the input current.

2. System Model

2.1. Design of the Active Joint. Figure 1 displays the schematic of the joint mechanism, which mainly comprises a double-magnetic-turntable rotor and stator. In the stator, six coils, which are grouped into EM1, EM2, and EM3, each of which is outfitted using a magnetic yoke. The stator is fixed in part to the housing. The rotor comprises double magnet discs with embedded type layout, which are arranged on the bilateral coil sides symmetrically. For each disc, four permanent magnets are assigned sequentially, and a magnet-plate yoke is used to outfit each disc to mitigate magnetic leakage. The adjoining permanent magnets exhibit magnetic poles of opposite directions. The sector permanent magnet forms a small air gap (only 1.7 mm) with the yoke, which allows the establishment of a uniform and high magnetic flux density at the air gap between two magnetic discs. The joint mechanism actuation is possible using the axial magnetic field through the permanent magnet-electromagnet interaction.

2.2. Modeling of the Joint Driving Torque. In this research, three sets of electromagnetic coils are assumed to be static, whereas the permanent magnet turntables are assumed to be mobile. Accordingly, following Newton's law of motion, the joint driving torque τ can be formulated as follows [32–35]:

$$\tau = 2IN_{ac}N_{\text{turn}}B_z\overline{R}l_e, \tag{1}$$

where I refers to the input current of the coil; N_{ac} and N_{turn} denote the number and turns of the coil, respectively; $\overline{R}$ indicates the equivalent radius of the magnet plate, where $\overline{R} = (R_1 + R_2)/2$, with R_1 and R_2 representing the inner and outer magnet radii, respectively; l_e denotes the equivalent length of the coil; and B_z is the air gap flux density. For the equation of the joint driving torque, the structural parameters of the joint mechanism are illustrated in Figure 2. The specific deduction process of equation (1) is presented in detail in reference [34].

2.3. Modeling of the Large Flexible Appendage System. Consider a large flexible appendage system comprising an active joint and a flexible appendage as displayed in Figure 3. The flexible appendage is assumed to be slender, and the rotary mass moment of inertia of cross section as well as shear deformation was not considered. The deflection of the flexible appendage is deemed small, and the gravity action is ignored. Here, τ is the external torque and θ is the angular displacement of the joint.
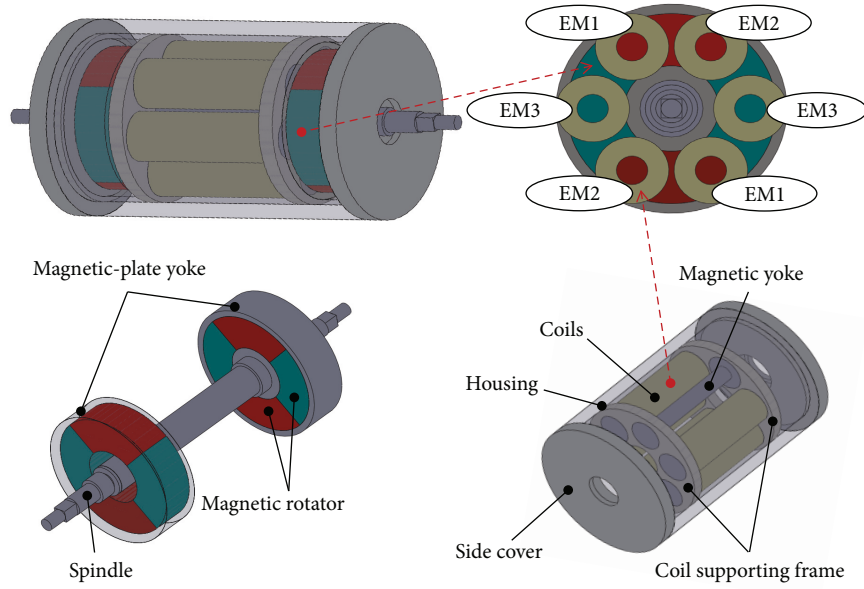
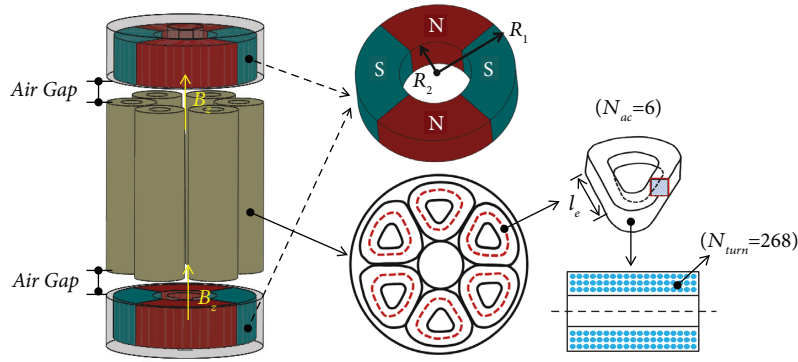FIGURE 1: Conceptual scheme of the joint mechanism.

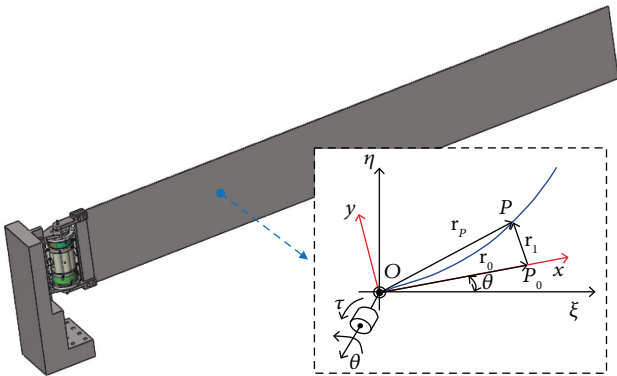FIGURE 2: Structural parameters of the joint mechanism.

FIGURE 3: Configuration of a large flexible rectangular appendage.

In accordance with Lagrange's method, the following differential equations should be satisfied using a dynamic system that is completely positioned using generalized coordinate q_i:

$$\frac{\mathrm{d}}{\mathrm{d}t}\left(\frac{\partial L}{\partial \dot{q}_i}\right) - \frac{\partial L}{\partial q_i} = Q_i, \quad i = 0, 1, 2, \ldots, \tag{2}$$

where L is the so-called Lagrangian expressed as follows:

$$L = T - V, \tag{3}$$

where T and V denote the kinetic and potential energies of the modeled system, respectively. Furthermore, Q_i refers to the generalized external force imposed on the relevant co-ordinate q_i.

Figure 3 illustrates the deformation of P, an arbitrary point (P), on the appendage. The constant inertial frame is represented by the coordinates $O\xi\eta$ [36]. In the local system of coordinates Oxy, which is fixed to the appendage, the position of P_0 is x away from the origin of the frame in the Ox direction. The movement of P_0 to the P location is noted following the displacements. The location vector of P can be expressed as follows:

$$\mathbf{r}_P = A\left(\mathbf{r}_0 + \mathbf{r}_1\right), \tag{4}$$

where $\mathbf{r}_0 = [x \, 0]^T$ denotes P_0's location vector in the O_{xy} frame and $\mathbf{r}_1 = [v(x,t) \, u(x,t)]^T$ denotes the P_0 to P location vector in the same frame, with $v(x,t)$ and $u(x, t)$ representing the axial and transverse deformations of the appendage, respectively. Typically, $v(x,t)$ is considerably smaller than $u(x,t)$. Thus, $v(x,t)$ is assumed to be negligible. In this case, $\mathbf{r}_1 = [0 \, u(x,t)]^T$ can be considered. The conversion matrix of Oxy to $O\xi\eta$ is expressed as follows:

$$A = \begin{bmatrix} \cos\theta & -\sin\theta \\ \sin\theta & \cos\theta \end{bmatrix}. \tag{5}$$

The velocity of P can be expressed as follows:

$$\frac{\partial \mathbf{r}_P}{\partial t} = \frac{\partial A}{\partial t}(\mathbf{r}_0 + \mathbf{r}_1) + A\frac{\partial \mathbf{r}_1}{\partial t}. \tag{6}$$

Thus, the kinetic energy of the system can be expressed as follows:

$$T = \frac{1}{2}J\dot{\theta}^2 + \frac{1}{2}\int_0^L \rho A\left(\frac{\partial \mathbf{r}_P}{\partial t}\right)^T \frac{\partial \mathbf{r}_P}{\partial t}dx, \tag{7}$$

where ρ denotes the mass density of the plate and J denotes the inertia moment of the joint.

The computational formula for the system's potential energy is expressed as follows:

$$V = \frac{1}{2}\int_0^L EI\left(\frac{\partial^2 u}{\partial x^2}\right)^2 dx, \tag{8}$$

where E denotes Young's modulus of the appendage and I denotes its geometrical inertia moment.

By using the assumed modes method, the appendage's elastic displacement $u(x,t)$ can be described as the linear combination of mode shapes $\phi(x)$ multiplied by the generalized time-related coordinates $\mathbf{q}(t)$ as follows:

$$u(x,t) = \phi(x)\mathbf{q}(t), \tag{9}$$

where $\phi(x)$ and $\mathbf{q}(t)$ denote the $1 \times N$ and $N \times 1$ vectors, respectively, which are expressed as follows:

$$\begin{aligned} \phi(x) &= [\varphi_1(x) \ \varphi_2(x) \ \cdots \ \varphi_N(x)], \\ \mathbf{q}(t) &= [q_1(t) \ q_2(t) \ \cdots \ q_N(t)]^T, \end{aligned} \tag{10}$$

where $\phi(x)$ is the mode shape function. The boundary conditions of the flexible appendage are as follows.

At $x = 0$,

$$u(0,t) = 0; \tag{11}$$
$$\frac{\partial u(0,t)}{\partial x} = 0.$$

At $x = l$,

$$EI\frac{\partial^2 u(l,t)}{\partial x^2} = 0,$$
$$EI\frac{\partial^3 u(l,t)}{\partial x^3} = 0. \tag{12}$$

For the dynamic equations of the coupling system of the flexible appendage and joint mechanism, both the kinetic energy T presented in equation (7) and the potential energy V given in equation (8) can be expressed using mode shapes together with the generalized coordinates provided in equation (9). Then, by using Lagrange's equation (equation (2)), the dynamic equations of the coupling system can be obtained from equations (7)–(12):

$$\mathbf{M}\ddot{x} + \mathbf{K}x + \mathbf{h}(\dot{\theta}, \theta, \dot{q}, q) = \mathbf{Q}, \tag{13}$$

where $\mathbf{x} = [\theta \, q_1 \ \ldots \ q_N]^T$ is the displacement vector; $\mathbf{Q} = [\tau(t) \, 0, \ \ldots, 0]^T$ refers to the generalized force; $\tau(t)$ represents the output torque of the joint mechanism; and $\mathbf{M}$, $\mathbf{K}$, and $\mathbf{h}$ are the mass matrix, stiffening matrix, and nonlinear force, respectively.

$$\begin{aligned} \mathbf{M} &= \begin{bmatrix} J & M_{e1} & \cdots & M_{eN} \\ M_{e1} & M_1 & \cdots & 0 \\ \vdots & \vdots & \vdots & \\ M_{eN} & 0 & \cdots & M_N \end{bmatrix}, \\ \mathbf{K} &= \begin{bmatrix} k & 0 & \cdots & 0 \\ 0 & K_1 & \cdots & 0 \\ \vdots & \vdots & \vdots & \\ 0 & 0 & \cdots & K_N \end{bmatrix}, \\ \mathbf{h} &= \begin{bmatrix} h_0(\dot{\theta}, \theta, \dot{q}, q) \\ h_1(\dot{\theta}, \theta, \dot{q}, q) \\ \vdots \\ h_N(\dot{\theta}, \theta, \dot{q}, q) \end{bmatrix}, \end{aligned} \tag{14}$$

where the variables of the mass matrix $\mathbf{M}$ can be expressed as follows:

$$J = \frac{1}{3}\rho Al^3 + \sum_{i=1}^N \left(\rho A \int_0^l W_i^2(x)dx \cdot q_i^2(t)\right),$$

$$M_{ei} = \rho A \int_0^l W_i(x)x dx,$$

$$M_i = \rho A \int_0^l W_i^2(x)dx,$$

$$K_i = EI \int_0^l \left[\frac{d^2 W_i(x)}{dx^2}\right]^2 dx,$$

$$h_0(\dot{\theta}, \theta, \dot{q}, q) = 2\rho A\left(\int_0^l W_i^2(x)dx \cdot q_i(t)\dot{q}_i(t)\right)\dot{\theta},$$

$$h_i(\dot{\theta}, \theta, \dot{q}, q) = -\rho A\left(\int_0^l W_i^2(x)dx q_i(t)\right)\dot{\theta}^2,$$

$$i = 1, 2, \ldots, N. \tag{15}$$

3. Vibration Control Simulations

3.1. Simulations of the Joint Driving Torque. Table 1 presents the geometric variables and material traits of the aluminum plate, where the appendage structural damping is disregarded. Table 2 presents the structural variables of the joint mechanism. The simulation was conducted according to the joint driving torque model in Section 2.2. The starting position and the rotation direction of the articulated stator and rotor are shown in Figure 4. The driving torque characteristics of the joint are shown in Figure 5.

The simulation results findings revealed the following:

(a) In 0°–40°, when the coils were supplied with DC-6 A power, the maximum output torque was 0.29 Nm. Within this rotation angle range, the joint driving torque remained nearly constant, and the torque was the largest. In addition, the driving torque grew linearly with the increase in the coil input current. The output torque of the joint mechanism was proportional to the input current. Therefore, in 0°–40°, the active control method could be used to actively suppress system vibrations. When the system was subjected to periodic excitation disturbance, the joint was used to output the torque of the same frequency but in the opposite direction to reduce the vibrations of space structures. The real-time angular displacement feedback was used to control the input current.

(b) At the angle of 60°, the driving torque was zero, and the joint output torque showed a nearly linear relationship with the rotation angle of 50°–70°, suggesting that the joint torsional stiffness was almost constant. Therefore, when DC supply was provided, the joint showed the characteristic of variable stiffness at this equilibrium position (60°). When the frequency of external stimulation approached the system's resonance frequency, the joint torsional stiffness could be changed by modulating the electric current, resulting in the frequency-shift phenomenon. Consequently, the isolation effect was realized. Therefore, the joint mechanism offered the potential for semi-active vibration control based on varying stiffness characteristics. However, in this study, the focus was not on semi-active control but on the active vibration control method.

3.2. Simulations of the System Vibration Control. The vibration of space flexible appendage mainly exhibits frequencies lower than 1 Hz. Therefore, in this study, the simulations were conducted to theoretically verify the low-frequency vibration suppression effect of the flexible appendage at less than 1 Hz and to further guide the structural design of the active joint.

To detail the vibration inhibitory efficiency of the active joint, a sinusoidal disturbance torque was utilized. The external disturbance amplitude was set to 0.01 Nm, and the disturbance frequencies were 0.2, 0.4, 0.6, and 0.8 Hz.

To suppress the low-frequency vibration, just simple algorithm for P control is adopted. In the case of the appendage disturbance by sinusoidal stimulation, the input current is controlled based on the real-time feedback of the angular displacement. The expression for the input current of the joint can be $I = k_p(\theta_d - \theta)$, where k_p is the proportional gain of the P controller, and the desired position of the joint is $\theta_d = 0$. The output torque of the joint mechanism is proportional to the input current, and the relationship between them can be obtained using equation (1).

The comparison of various proportional gains is presented with numerical simulation results. According to the simulation results in Figure 6, the flexible structure vibration can be reduced to small amplitudes. The larger the excitation frequency is, the smaller the amplitude is, and the proposed active joint exhibits a suitable and an efficient performance to inhibit the appendage's low-frequency vibration just by using the simple P control algorithm. The larger the proportional gain is, the superior the vibration inhibitory efficiency is and the more the energy consumption of the joint mechanism is.

4. Vibration Control Experiments

Spacecraft in space is typically affected by various complex disturbances, resulting in low-frequency vibration of space flexible appendages. Although simulating diverse interference sources during the ground experiment is difficult, equivalent external perturbation in space can be obtained by introducing some typical periodic excitations to study low-frequency vibration isolation performance.

4.1. Vibration Control Experiments under Single-Frequency Excitation. For the functionality validation of the designed active joint mechanism, as displayed in Figure 7, an experimental platform based on rotary flexible appendage was constructed and a self-fabricated stimulator for electromagnetic noncontact periodic excitations was developed along the direction of rotation. One permanent magnet (PM1) was attached to the output shaft of the servo motor and bonded the other (PM2) to the connecting member of the joint mechanism. The two PMs were kept almost 1 mm apart regarding air gap. The motor output angular velocity and displacement based on the PM1–PM2 interaction were regulated, which enabled production of sinusoidal stimulation for experimentation within a certain frequency band, such as varying amplitudes and frequencies.

Figure 8 depicts the block diagram of the experimental system. During the experiments, the low-frequency signal of sinusoidal perturbation, which is stimulated by electromagnetic noncontact periodic excitation, is exerted on the large appendage. The desired angle position θ_d is 0. The applied current is proportional to the error signal. The input current is controlled using the real-time feedback of angular displacement. If the appendage is interfered with periodic stimulation, the joint inhibits the appendage vibration by outputting identical frequency and reverse directional

TABLE 1: Mechanism parameters of the rotational flexible appendage.

Length (L)	Thickness (h)	Width (b)	Elastic modulus (E)	Density (ρ)
1088 mm	1.5 mm	130 mm	69 GPa	2766 kg/m^3

TABLE 2: Structural parameters of the joint mechanism.

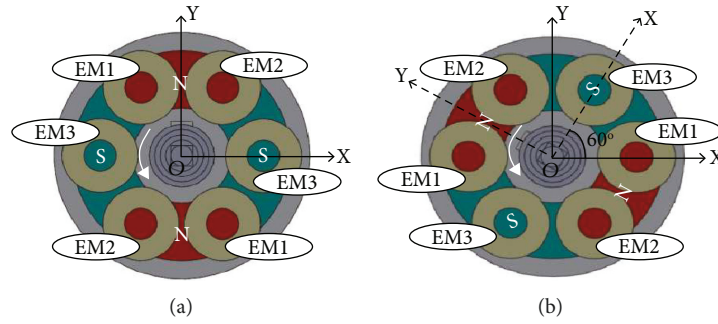| Total size (mm)	Total weight (kg)	Coil size (mm)	Coil turns
$\Phi 55 \times 91$	0.77	$\Phi 6 \times \Phi 14 \times 40$	268
Resistance (Ω)	Current (A)	Permanent magnet	
0.76	0–6	NdFeB35	

FIGURE 4: Relative rotation direction of the coil stator and the permanent magnet rotor: (a) initial position of the coil stator and the permanent magnet rotor and (b) the permanent magnet rotor rotating to 60°.
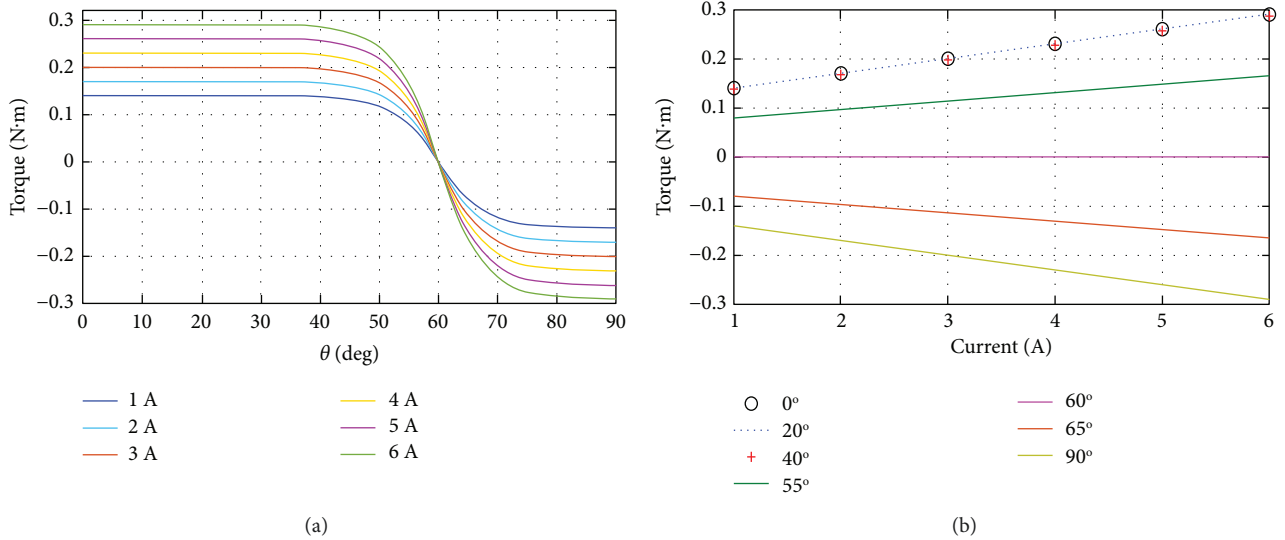

FIGURE 5: Simulation results of the driving torque characteristics of the joint: (a) torque-angle relationships at different currents and (b) torque-current relationships at different angles.

torque. The sampling period is 1 ms. Two sets of experiments were conducted, namely Experiments **I** and **II**.

For the excitations of same frequency but distinct amplitudes in Experiment **I**, the time domain and frequency domain responses are displayed in Figure 9. Considering Figure 9(a) as an example, the perturbation signal has a primary frequency of 0.26 Hz. For the proportional gain k_p

of 0.02, the amplitude with control in time domain decreased from −2.40°–2.39° to −1.44°–1.34°. The amplitude with control in the frequency domain was suppressed from 2.26° to 1.05°, with 53.54% isolating effect and 6.66 dB attenuation. For control gain k_p of 0.03, the results revealed a decline of the amplitude with control in the temporal domain to −0.27°–0.31° from −2.40°–2.39°. The amplitude with control
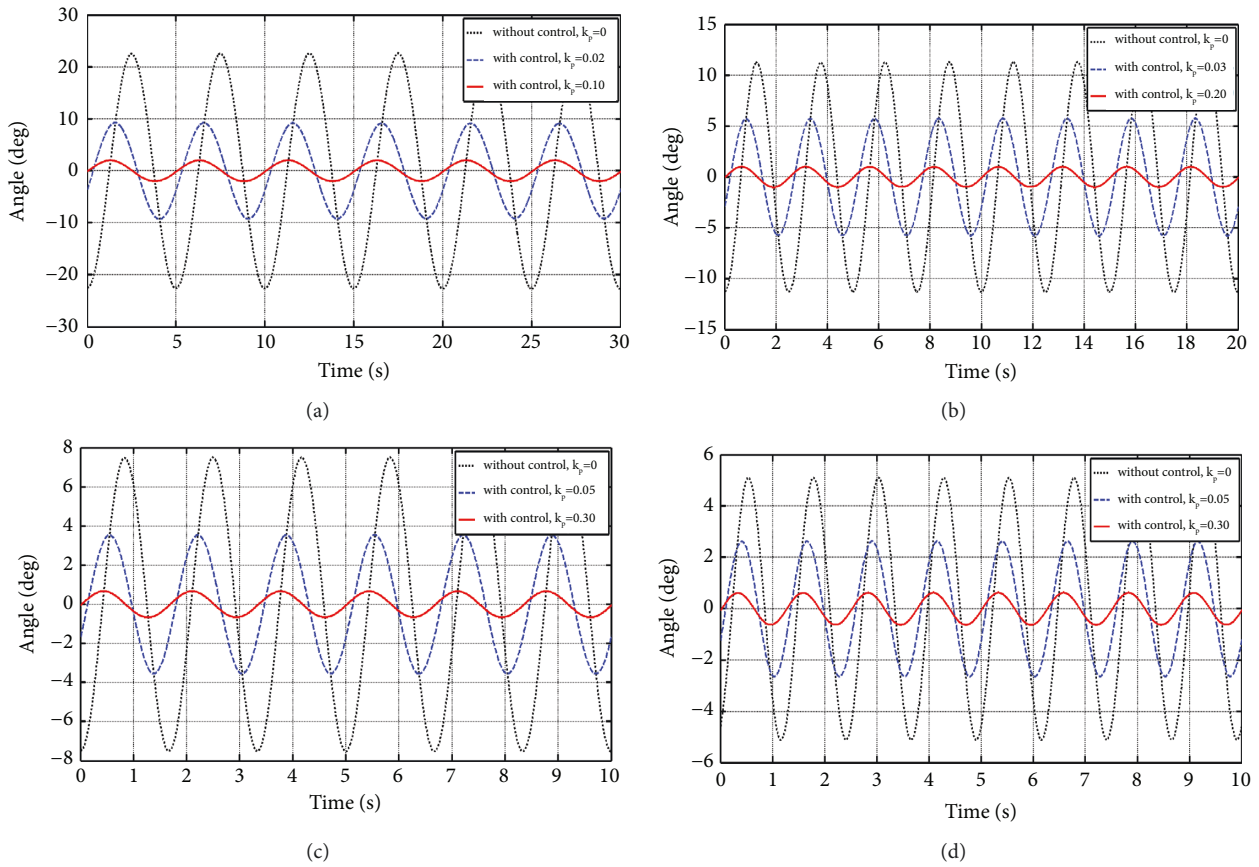
FIGURE 6: Simulation results of vibration control excitation at (a) 0.2, (b) 0.4, (c) 0.6, and (d) 0.8 Hz.
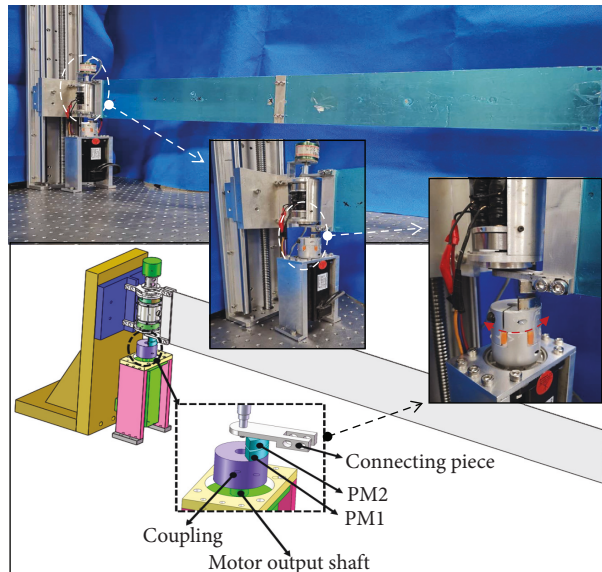

FIGURE 7: Experiment test setup diagram under electromagnetic noncontact periodic excitation.

in the frequency domain is attenuated from 2.26° to 0.16°, which indicates a decrease of 92.92%, corresponding to 23 dB suppression. Subsequently, based on the real-time feedback of angular displacement, the input current was adjusted to achieve active vibration isolation. The three sets of coils had the same input current, and the root mean
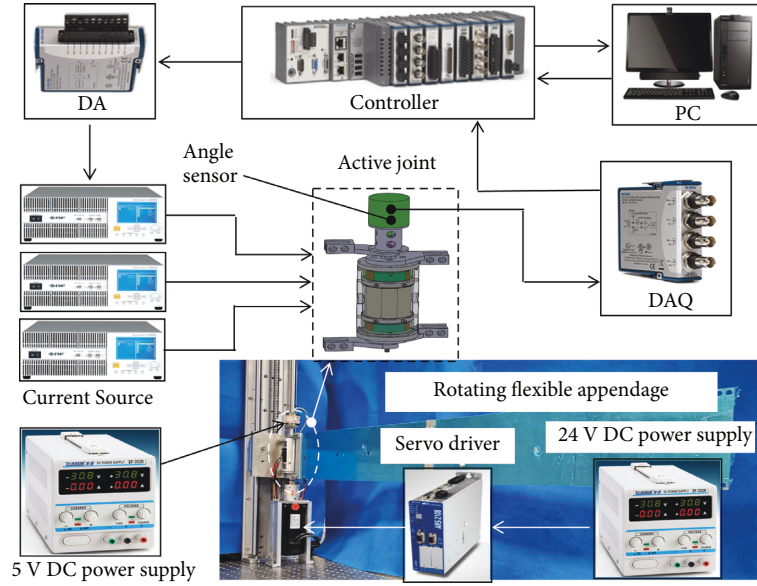
FIGURE 8: Test platform.

square of the input current in each coil was 0.431 A. Next, in Figures 9(b) and 9(c), the same analytical procedures were performed. The experiment results are listed in Table 3. The minimum control scope of amplitude exhibits a decrease to $-0.27°$–$0.31°$ (peak-to-peak $0.58°$) from $-2.40°$–$2.39°$ (peak-to-peak $4.79°$), whereas the maximum control scope exhibits repression to $-0.67°$–$1.06°$ (peak-to-peak $1.73°$) from $-14.33°$–$15.28°$ (peak-to-peak $29.61°$). The frequency of perturbation almost remained unchanged (0.26 Hz), and the amplitude varied, with the vibration attenuation of 23–32.41 dB. As indicated by the experimental findings, the vibration prominently diminished merely by the simple P control algorithm, particularly in the case of large-amplitude vibrations at low frequencies. The larger the proportional gain was, the better the isolation effect was, and the larger current required. The best vibration isolation effect up to 97.60% was achieved in Experiment **I (b)**.

For the excitations of various frequencies and amplitudes in Experiment **II**, the time- and frequency-domain response are displayed in Figure 10. In Figure 10(a), the perturbation signal has a primary frequency of 0.46 Hz. For proportional gain k_p of 0.10, the amplitude with control in time domain decreased from $-4.30°$–$4.33°$ to $-2.78°$–$2.82°$; the amplitude with control in the frequency domain was suppressed from $3.90°$ to $2.53°$, with 35.13% isolating effect and 3.76 dB attenuation. For k_p of 0.30, the results revealed a decline in the amplitude with control in the temporal domain from $-4.30°$–$4.33°$ to $-1.32°$–$0.93°$. The amplitude with control in the frequency domain was attenuated from $3.9°$ to $0.69°$, with a decrease of 82.31%, which corresponded to 15.04 dB suppression. The root mean square of the joint input current was 1.479 A. Next, in Figures 10(b) and 10(c), the same analytical procedures were performed. The experiment results are listed in Table 4, the control scope of amplitude exhibits a decrease to $-0.30°$–$0.29°$ (peak-to-peak $0.59°$) from $-0.98°$–$0.90°$ (peak-to-peak $1.88°$), whereas the

maximum control scope exhibits the decrease to $-1.32°$–$0.93°$ (peak-to-peak $2.25°$) from $-4.30°$–$4.33°$ (peak-to-peak $8.63°$). The perturbation signal exhibited a primary frequency bandwidth of 0.46–0.63 Hz, whereas, the vibration attenuation ranged between 12.26 and 15.04 dB within the valid bandwidth. The larger the excitation frequency is, the smaller the amplitude is. As detailed by the foregoing findings, the inhibition of vibrations with smaller amplitudes is possible, and the control strategy is simple and easy to implement.

In Section 4.1, the rotational vibration of flexible appendage can be frequently excited by the external non-contact disturbances with single-frequency periodic excitation. The joint input current was adjusted to actively maintain the real-time feedback of angular displacement to suppress the vibration of the appendage. The experimental results revealed that for the single-frequency excitation, even with the simple P control algorithm, the proposed joint mechanism effectively suppressed both the larger and the smaller amplitude vibrations at low frequency. The perturbation signal exhibited a primary frequency bandwidth of 0.26–0.63 Hz, where the vibration attenuation ranged between 12.26 and 32.41 dB in effective bandwidth.

4.2. Vibration Control Experiments under Multi-frequency Stimulations.

Two regular shaking head fans with adjustable 2 to 3 power levels are applied for simulating the periodic noncontact stimulations at multi-frequencies, as displayed in Figure 11. During the experiments, the fans were located on the bilateral sides of the flexible appendage. Through differing in modes of combination, varying perturbation traits can be derived. Four cases were provided to illustrate the vibration isolation efficiency of the proposed actuator under two fans airflow periodic excitation, as presented in Table 5. Although this excitation method is simple, the appendages random perturbation was presented accurately.
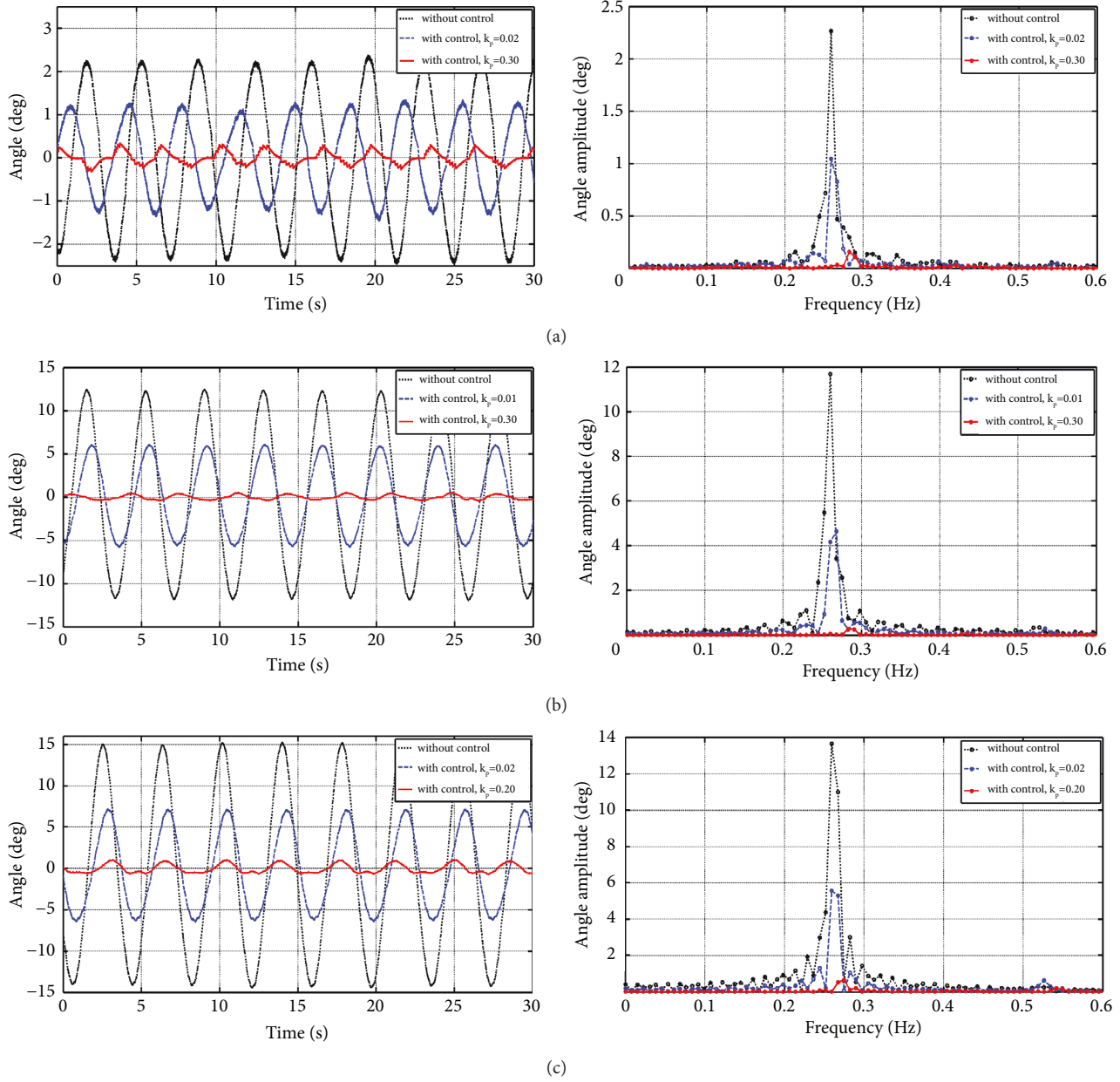
Figure 9: Vibration control Experiment **I** excitation at 0.26 Hz.

Table 3: Vibration control effect based on the novel active joint in Experiment **I**.

| Experiment **I**		Amplitude (°)		Major frequency	Current (RMS)
(a)	Without control ($k_p = 0$)	−2.40°–2.39°	Amplitude (°)	0.26 Hz 2.26°	0 A
	With control ($k_p = 0.3$)	−0.27°–0.31°	Amplitude (°) Control effect (%) Control effect (dB)	0.16° 92.92% −23.00 dB	0.431 A
(b)	Without control ($k_p = 0$)	−11.79°–12.26°	Amplitude (°)	0.26 Hz 11.69°	0 A
	With control ($k_p = 0.3$)	−0.43°–0.57°	Amplitude (°) Control effect (%) Control effect (dB)	0.28° 97.60% −32.41 dB	0.776 A
(c)	Without control ($k_p = 0$)	−14.33°–15.28°	Amplitude (°)	0.26 Hz 13.67°	0 A
	With control ($k_p = 0.2$)	−0.67°–1.06°	Amplitude (°) Control effect (%) Control effect (dB)	0.66° 95.17% −26.32 dB	1.093 A

(a)

(b)

(c)
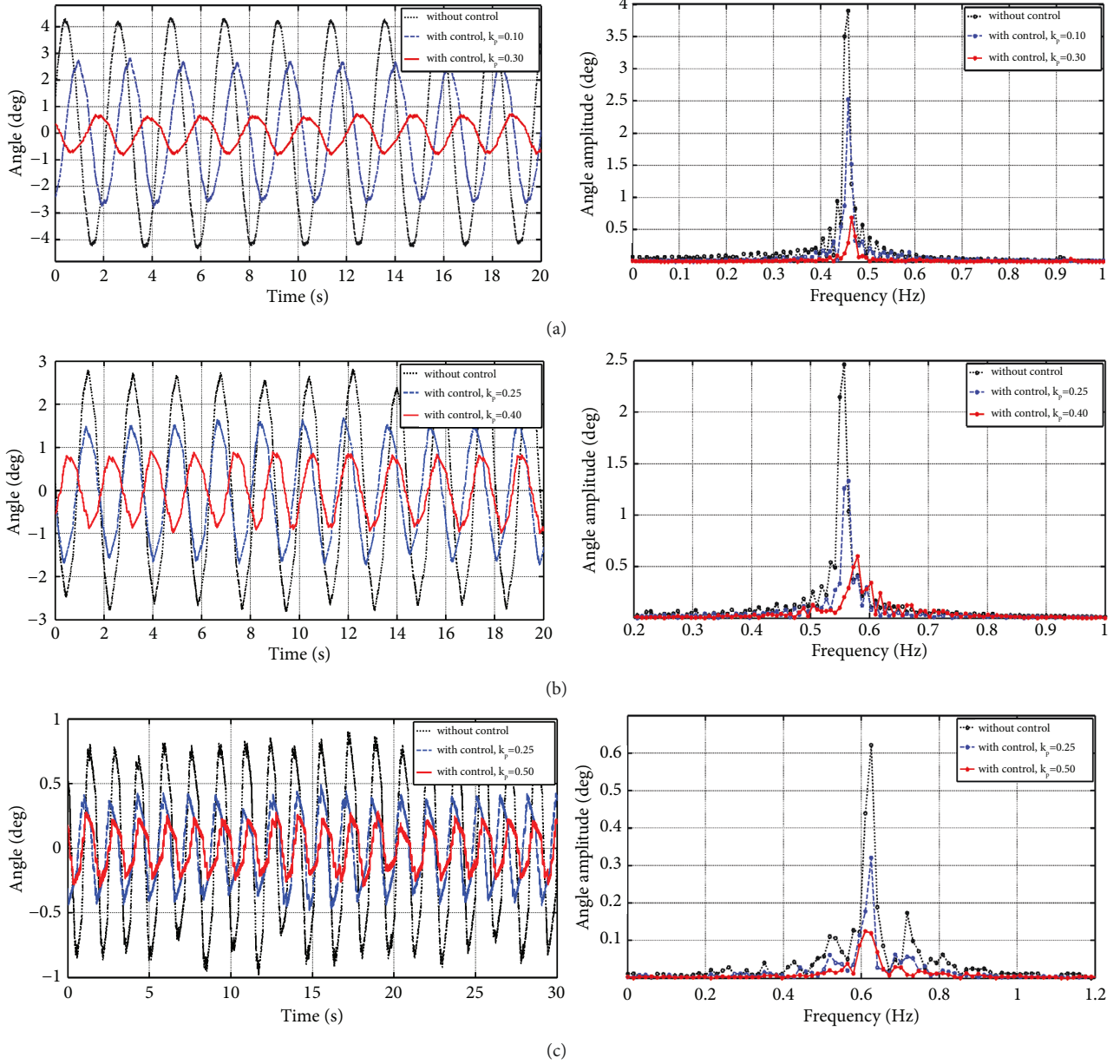
FIGURE 10: Vibration control Experiment **II** excitation at (a) 0.46, (b) 0.56, and (c) 0.63 Hz.

In Experiment **I**, as illustrated in Figure 12(a), for k_p of 0.05, the amplitude under active control decreased from −11.97°–9.99° to −5.78°–5.84°, the primary frequencies of perturbation signal were 0.08 and 0.17 Hz, respectively, the vibration amplitude was weakened under active control from 3.22° to 2.64°, and 3.17° to 1.84°, with 18.01% (−1.73 dB) and 53.31% (−6.62 dB) isolation effect, respectively. For current k_p of 0.20, the amplitude declined from −11.97°–9.99° to −3.13°–2.34° under active control. The vibration amplitude was weakened under active control from 3.22° to 1.07° at 0.08 Hz and 3.17° to 0.48° at 0.17 Hz, with 66.67% (−9.57 dB) and 84.86% (−14.60 dB) isolation effect, respectively. Furthermore, the higher was the proportional gain, the more obvious was the active control effect. In Experiment **II**, the

isolation effect is discussed following the same analytical procedures. Figure 12(b) displays the perturbation signal and control efficiency, and Table 6 details the two groups of experimental results.

According to the single-frequency stimulation strategy, in the process of mutual driving between the two PMs, passive damping effect is produced and vibration isolation may be achieved. Therefore, to prove that the actual isolation effect was achieved by the proposed joint mechanism rather than passive damping, Experiments **III** and **IV** were performed. As displayed in Figure 13, the motor output shaft was locked, and PM1 remained stationary.

In Experiment **III**, as illustrated in Figure 14(a), for k_p of 0.05, the amplitude declined under active control from

TABLE 4: Vibration control effect based on the novel active joint in Experiment **II**.

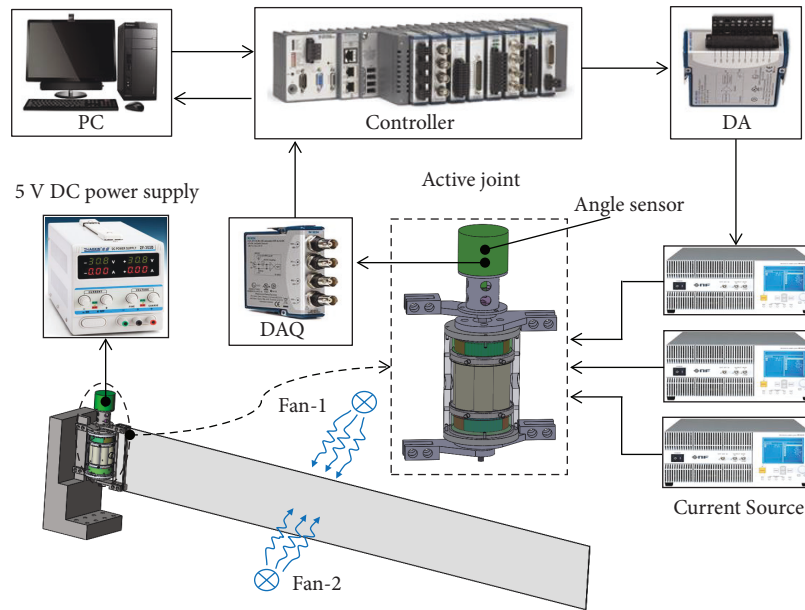| Experiment **II**		Amplitude (°)			Major frequency	Current (RMS)
(a)	Without control ($k_p = 0$)	−4.30°–4.33°	Amplitude (°)		0.46 Hz 3.90°	0 A
	With control ($k_p = 0.30$)	−1.32°–0.93°	Amplitude (°) Control effect (%) Control effect (dB)		0.69° 82.31% −15.04 dB	1.479 A
(b)	Without control ($k_p = 0$)	−2.82°–2.81°	Amplitude (°)		0.56 Hz 2.46°	0 A
	With control ($k_p = 0.40$)	−0.97°–0.91°	Amplitude (°) Control effect (%) Control effect (dB)		0.60° 75.61% −12.26 dB	2.237 A
(c)	Without control ($k_p = 0$)	−0.98°–0.90°	Amplitude (°)		0.63 Hz 0.62°	0 A
	With control ($k_p = 0.50$)	−0.30°–0.29°	Amplitude (°) Control effect (%) Control effect (dB)		0.13° 79.03% −13.57 dB	0.768 A

FIGURE 11: Experimental setup of periodic stimulations based on two fans.

TABLE 5: Varying modes of shaking head fan combinations.

Experiments	Different combinations
I	Two high-power fans, with one being the shaking head type and the other not shaking its head, are utilized, whose distance from the appendage is kept constant
II	One high-power shaking head fan and one low-power fan not shaking its head, are utilized, whose distance from the appendage is kept constant
III	Passive damper is incorporated on the basis of Experiment **I**
IV	Passive damper is incorporated on the basis of Experiment **II**

−5.83°–4.76° to −4.14°–3.15°. The vibration amplitude weakened under active control from 1.37° to 1.23° at 0.08 Hz, and 1.06° to 0.96° at 0.17 Hz, showing a decrease of 10.22% (−0.94 dB) and 9.4% (−0.86 dB), respectively. For k_p of 0.20, the amplitude under active control decreased from −5.83°–4.76° to −2.18°–1.63°. The vibration amplitude weakened under active control from 1.37° to 0.67° at 0.08 Hz and 1.06° to 0.43°at 0.17 Hz, showing a decrease of 51.09% (−6.21 dB) and 59.43% (−7.84 dB), respectively. The higher was the proportional gain, the more obvious was the active control effect. In Experiment **IV**, the active control effect was studied using the same analytical procedure. Figure 14(b) displays the perturbation signal and control efficiency, and Table 7 details relevant summarizations. As suggested by the
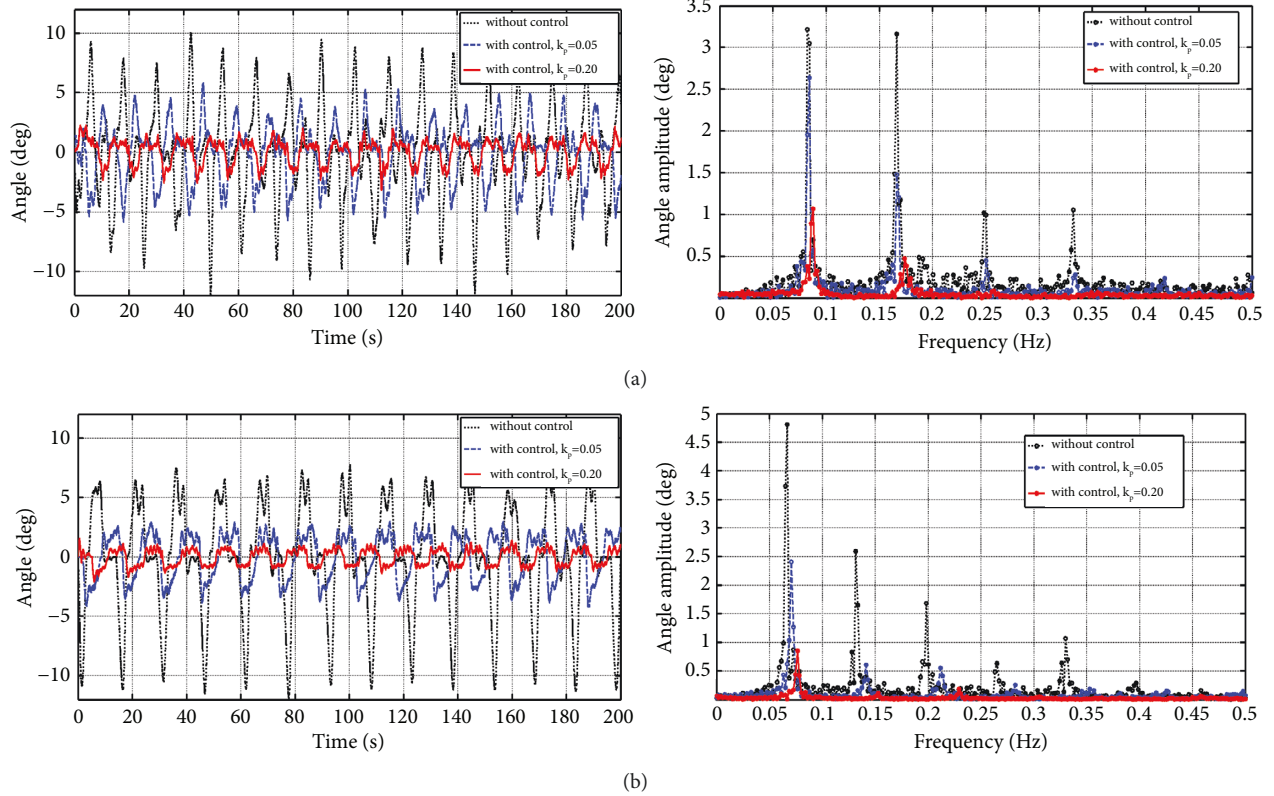
FIGURE 12: Vibration control experiments: (a) Experiment **I**; (b) Experiment **II**.

TABLE 6: Vibration control effect in Experiments **I** and **II**.

Experiments		Amplitude (°)		Major frequency		Current (RMS)
I	Without control ($k_p = 0$)	–11.97°–9.99°	Amplitude (°)	0.08 Hz 3.22°	0.17 Hz 3.17°	0 A
	With control ($k_p = 0.2$)	–3.13°–2.34°	Amplitude (°)	1.07°	0.48°	2.052 A
			Control effect (%)	66.77%	84.86%	
			Control effect (dB)	–9.57 dB	–16.40 dB	
II	Without control ($k_p = 0$)	–11.49°–7.58°	Amplitude (°)	0.07 Hz 4.81°	0.13 Hz 2.60°	0 A
	With control ($k_p = 0.2$)	–2.06°–1.59°	Amplitude (°)	0.86°	0.11°	1.358 A
			Control effect (%)	82.12%	95.77%	
			Control effect (dB)	–14.95 dB	–27.47 dB	

results of fans airflow stimulation-based experimentation, the passive damper was efficient under severe vibrations. Thus, the experimental comparison results revealed the advantages and the robustness of the proposed method.

In Section 4.2, for multi-frequency excitations, four groups of experiments were conducted. The perturbation signal has a primary frequency bandwidth of 0.07–0.17 Hz, where the vibration attenuation is prominent between 5.95 and 27.47 dB within the valid bandwidth. Higher proportional gain indicates efficient vibration inhibition. The optimal efficiency of the vibration inhibition can be up to 95.77% at 0.13 Hz in Experiment **II**. Moreover, the novel active joint probably allows repression of vibrations with large amplitudes at low frequencies to some extent. Throughout the aforementioned experiments, the simple P

control proved to be a promising and versatile control technique based on the proposed active joint mechanism.

For the external disturbances/noises introduced by the bilateral fan, it is difficult to use only a single fan to simulate low-frequency periodic reciprocating disturbances along the rotation direction. Therefore, two fans are attached onto both the sides of the flexible appendage; one is a shaking-head-type fan, and the other fan does not shake its head. The noncontact airflow force generated by the two fans acts on the surface of the flexible appendage, and then, the periodic interference is obtained. Furthermore, different interference characteristics can be obtained by varying fan power combinations.

For these effects, the low-frequency rigid body angular vibration generated by the airflow excitation
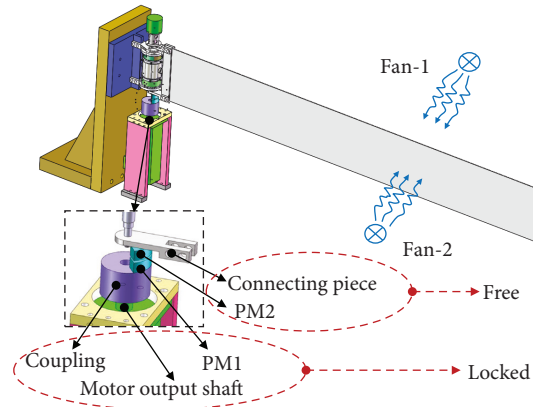
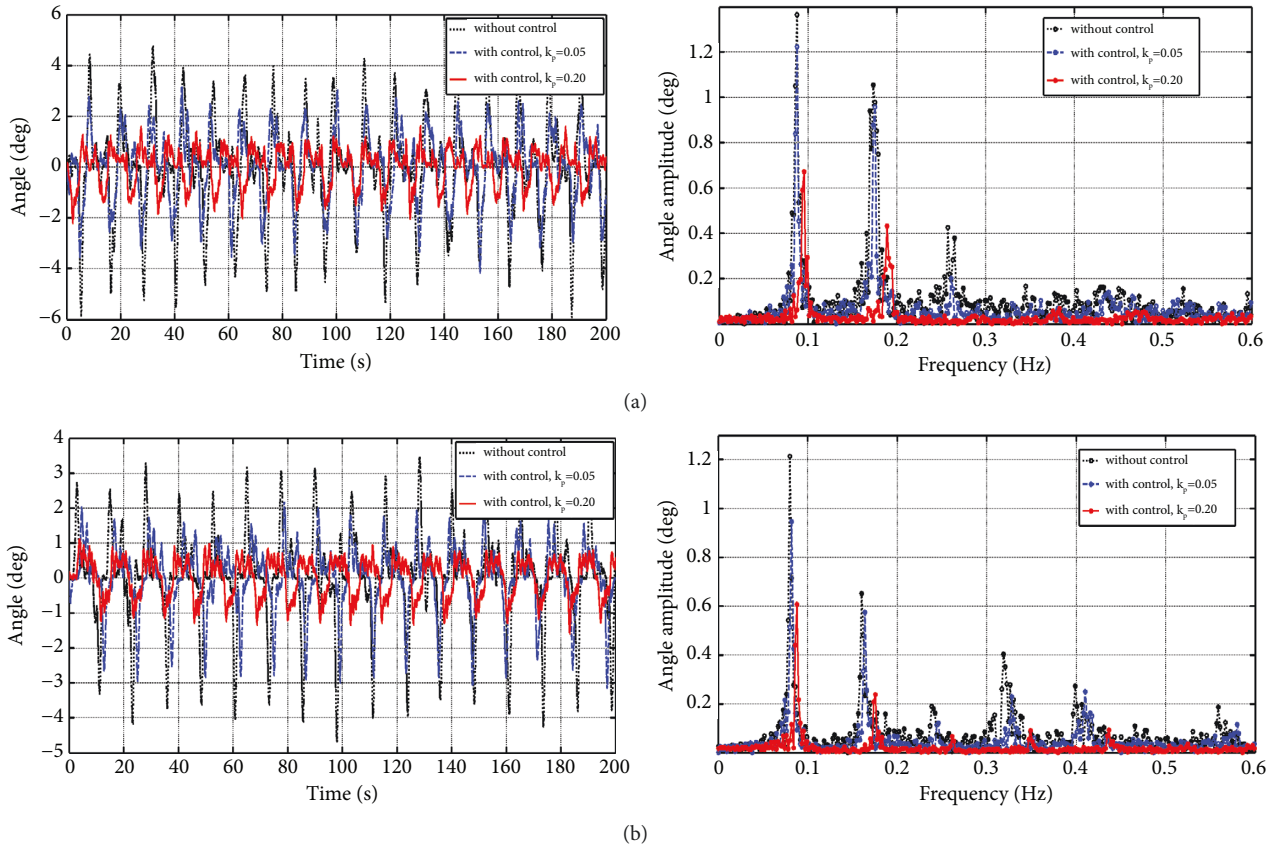FIGURE 13: Experiment test setup diagram with the periodic fan airflow stimulation and passive damping.

(a)

(b)

FIGURE 14: Vibration control experiments with passive damping: (a) Experiment **III**; (b) Experiment **IV.**

presents a multi-frequency phenomenon, mainly because the low-frequency rigid body angular vibration of the system is coupled with the elastic vibration generated by the flexible appendage. The first dominant frequency (approximately 0.08 Hz), that is, the frequency of the shaking head fan, represents the low-frequency rigid body angular vibration caused by this fan. However,

other dominant frequency components are the noise interferences caused by the elastic vibration generated by the flexible appendage, and the elastic vibration generated by the flexible appendage results from the angular motion of the rigid body of the system. The airflow excitation of the noncontact fans has a certain guiding importance for the experimental method of low- or ultra-

TABLE 7: Efficiencies of vibration control in the passive damping-based Experiments **III** and **IV**.

Experiments		Amplitude (°)		Major frequency		Current (RMS)
III	Without control ($k_p = 0$)	−5.83°–4.76°	Amplitude (°)	0.08 Hz 1.37°	0.17 Hz 1.06°	0 A
	With control ($k_p = 0.2$)	−2.18°–1.63°	Amplitude (°) Control effect (%) Control effect (dB)	0.67° 51.09% −6.21 dB	0.43° 59.43% −7.84 dB	1.470 A
IV	Without control ($k_p = 0$)	−4.66°–3.51°	Amplitude (°)	0.08 Hz 1.21°	0.16 Hz 0.65°	0 A
	With control ($k_p = 0.2$)	−1.35°–1.13°	Amplitude (°) Control effect (%) Control effect (dB)	0.61° 49.59% −5.95 dB	0.24° 63.08% −8.65 dB	1.058 A

low-frequency interference source simulation of space flexible appendages.

5. Conclusions

This study focused on the suppression of low-frequency vibration of a large flexible appendage. A novel active joint based on direct electromagnetic drive was proposed. The joint was mounted at the root of the flexible appendage and provides control actions to suppress both the larger and the smaller amplitude vibrations at low frequency.

In this study, modeling, simulation, and experimental validation of vibration control, based on a novel joint mechanism, were performed. For the proposed system, its motion equations are acquired based on the assumed-modes approach. Numerical predictions were verified through extensive comparisons. Two noncontact strategies were developed for periodic vibration stimulation along the rotation direction. A self-fabricated electromagnetic vibration stimulator was applied to the appendage root for single-frequency periodic stimulation. As displayed by the results, the perturbation signal exhibits a primary frequency bandwidth of 0.07–0.63 Hz, where the vibration attenuation was prominent between 5.95 and 27.47 dB within the valid bandwidth. Vibrations at low frequencies can be suppressed using the active joint, without additional intelligent material onto the appendage surface. Furthermore, the implementation of the P control scheme considerably attenuated vibration over the uncontrolled case. The numerical results and experimental findings revealed that the proposed joint mechanism exhibits robust vibration suppression at low-frequency ranges for large flexible appendage systems.

The prominent features of such a P-like controller include simple control, high reliability, high robustness, and easy implementation for the proposed joint mechanism, which is particularly suitable for aerospace applications.

However, this paper does not focus on the control algorithm but on the complete solution. The main contribution of this study is the method of low-frequency vibration control for space large flexible appendages with active joint mechanisms. This method has the advantage of electromagnetic direct drive. The spindle is directly linked to the load, and thus, the clearance and friction caused by intermediate transmissions are minimized. Furthermore, it presents the benefits of integrated structure and function design. It is not only a structural member but also a functional member. It acts as a structural component, providing support to neighboring appendages. It also behaves as a functional piece, which can achieve appendage vibration control. Furthermore, an active control algorithm was proposed, and the experimental results indicated that the control algorithm is feasible and easy to implement.

Currently, considerable efforts have been devoted to the structural design and ultimate prototyping of the joint mechanism; the P-like control algorithm provides only a preliminary functional verification. In the future research, we will focus on the intelligent control algorithms for the proposed joint mechanism to realize active vibration control of space flexible appendages highly effectively.

Data Availability

The raw data are available from the corresponding author upon request.

Conflicts of Interest

The authors declare that they have no conflicts of interest.

Acknowledgments

References

[1] E. Azadi, S. A. Fazelzadeh, and M. Azadi, "Thermally induced vibrations of smart solar panel in a low-orbit satellite," *Advances in Space Research*, vol. 59, no. 6, pp. 1502–1513, 2016.

[2] J. Liu and K. Pan, "Rigid-flexible-thermal coupling dynamic formulation for satellite and plate multibody system," *Aerospace Science and Technology*, vol. 52, no. 1, pp. 102–114, 2016.

[3] L. Liu, D. Cao, H. Huang, C. Shao, and Y. Xu, "Thermal-structural analysis for an attitude maneuvering flexible spacecraft under solar radiation," *International Journal of Mechanical Sciences*, vol. 126, no. 1, pp. 161–170, 2017.

[4] D. Li, J. Jiang, W. Liu, and C. Fan, "A new mechanism for the vibration control of large flexible space structures with embedded smart devices," *IEEE*, vol. 20, no. 4, pp. 1653–1659, 2015.

[5] X. Cao, C. Yue, and M. Liu, "Flexible satellite attitude maneuver via constrained torque distribution and active vibration suppression," *Aerospace Science and Technology*, vol. 67, pp. 387–397, 2017.

[6] Z. Liu, J. Liu, and L. Wang, "Disturbance observer based attitude control for flexible spacecraft with input magnitude and rate constraints," *Aerospace Science and Technology*, vol. 72, pp. 486–492, 2018.

[7] J. R. Maly, B. B. Reed, M. J. Viens, and B. H. Parker, "Life cycle testing of viscoelastic materials for hubble space telescope solar array 3 damper," *Smart structures and materials 2003: damping and isolation. International Society for Optics and Photonics*, vol. 5052, pp. 128–141, 2003.

[8] Y. Kong and H. Huang, "Design and experiment of a passive damping device for the multi-panel solar array," *Advances in Mechanical Engineering*, vol. 9, no. 2, pp. 1–10, 2017.

[9] S. K. Dwivedy and P. Eberhard, "Dynamic analysis of flexible manipulators, a literature review," *Mechanism and Machine Theory*, vol. 41, no. 7, pp. 749–777, 2006.

[10] H. N. Rahimi and M. Nazemizadeh, "Dynamic analysis and intelligent control techniques for flexible manipulators: a review," *Advanced Robotics*, vol. 28, no. 2, pp. 63–76, 2014.

[11] K. Lochan, B. K. Roy, and B. Subudhi, "A review on two-link flexible manipulators," *Annual Reviews in Control*, vol. 42, pp. 346–367, 2016.

[12] S.-H. Lee and C.-W. Lee, "Hybrid control scheme for robust tracking of two-link flexible manipulator," *Journal of Intelligent and Robotic Systems*, vol. 32, no. 4, pp. 389–410, 2001.

[13] E. Mirzaee, M. Eghtesad, and S. A. Fazelzadeh, "Maneuver control and active vibration suppression of a two-link flexible arm using a hybrid variable structure/Lyapunov control design," *Acta Astronautica*, vol. 67, no. 9, pp. 1218–1232, 2010.

[14] S. K. Tso, T. W. Yang, W. L. Xu, and Z. Q. Sun, "Vibration control for a flexible-link robot arm with deflection feedback," *International Journal of Non-Linear Mechanics*, vol. 38, no. 1, pp. 51–62, 2003.

[15] O. Abdeljaber, O. Avci, and D. J. Inman, "Active vibration control of flexible cantilever plates using piezoelectric materials and artificial neural networks," *Journal of Sound and Vibration*, vol. 363, pp. 33–53, 2016.

[16] Z.-c. Qiu and S.-m. Zhang, "Fuzzy fast terminal sliding mode vibration control of a two-connected flexible plate using laser sensors," *Journal of Sound and Vibration*, vol. 380, pp. 51–77, 2016.

[17] Z.-c. Qiu, D.-f. Ling, X.-m. Zhang, and J.-d. Han, "Vibration control of two-connected piezoelectric flexible plate using nonlinear algorithm and T-S fuzzy controller," *Journal of Intelligent Material Systems and Structures*, vol. 26, no. 2, pp. 219–243, 2014.

[18] R. Xu, D. Li, and J. Jiang, "An online learning-based fuzzy control method for vibration control of smart solar panel," *Journal of Intelligent Material Systems and Structures*, vol. 26, no. 18, pp. 2547–2555, 2015.

[19] J. Lin and Y. B. Zheng, "Vibration suppression control of smart piezoelectric rotating truss structure by parallel neuro-fuzzy control with genetic algorithm tuning," *Journal of Sound and Vibration*, vol. 331, no. 16, pp. 3677–3694, 2012.

[20] J. Jiang and D. Li, "Optimal placement and decentralized robust vibration control for spacecraft smart solar panel structures," *Smart Materials and Structures*, vol. 19, no. 8, pp. 1–9, 2010.

[21] J.-P. Jiang and D.-X. Li, "Decentralized robust vibration control of smart structures with parameter uncertainties," *Journal of Intelligent Material Systems and Structures*, vol. 22, no. 2, pp. 137–147, 2011.

[22] Q. Zhu, J. Z. Yue, and W. Q. Liu, "Active vibration control for piezoelectricity cantilever beam: an adaptive feed-forward control method," *Smart Materials and Structures*, vol. 26, no. 4, pp. 1–13, 2017.

[23] B. Ma, Z.-c. Qiu, X.-m. Zhang, and J.-d. Han, "Experiments on resonant vibration suppression of a piezoelectric flexible clamped-clamped plate using filtered-U least mean square algorithm," *Journal of Intelligent Material Systems and Structures*, vol. 27, no. 2, pp. 166–194, 2016.

[24] P. Gasbarri, R. Monti, and M. Sabatini, "Very large space structures: non-linear control and robustness to structural uncertainties," *Acta Astronautica*, vol. 93, no. 1, pp. 252–265, 2014.

[25] Y. Xie, H. Shi, F. Bi, and J. Shi, "A MIMO data driven control to suppress structural vibrations," *Aerospace Science and Technology*, vol. 77, pp. 429–438, 2018.

[26] K. Yang, W. Tong, L. Lin, D. Yurchenko, and J. Wang, "Active vibration isolation performance of the bistable nonlinear electromagnetic actuator with the elastic boundary," *Journal of Sound and Vibration*, vol. 520, Article ID 116588, 2022.

[27] E. Eshraqi, M. Shahravi, M. Shahravi, and M. Azimi, "Consideration of spillover effect in active vibration suppression of a smart composite plate using piezoelectric elements," *Latin American Journal of Solids and Structures*, vol. 13, no. 14, pp. 2643–2656, 2016.

[28] M. Azimi, M. Shahravi, and K. M. Fard, "Modeling and vibration suppression of flexible spacecraft using higher-order sandwich panel theory," *International Journal of Acoustics and Vibration*, vol. 22, no. 2, pp. 143–151, 2017.

[29] L. Sievert, D. Stancioiu, and C. Matthews, "Active vibration control of a small-scale flexible structure subject to moving-loads and experimental validation," *Journal of Vibration and Acoustics*, vol. 143, no. 6, 2021.

[30] W. Hu, Y. Gao, and B. Yang, "Semi-active vibration control of two flexible plates using an innovative joint mechanism," *Mechanical Systems and Signal Processing*, vol. 130, pp. 565–584, 2019.

[31] M. Shahravi and M. Azimi, "A comparative study for collocated and non-collocated sensor/actuator placement in vibration control of a maneuvering flexible satellite," *Proceedings of the Institution of Mechanical Engineers—Part C: Journal of Mechanical Engineering Science*, vol. 229, no. 8, pp. 1415–1424, 2015.

[32] H. Kim, H. Kim, D. Ahn, and D. Gweon, "Design of a new type of spherical voice coil actuator," *Sensors and Actuators A: Physical*, vol. 203, no. 12, pp. 181–188, 2013.

[33] E. P. Furlani, *Permanent Magnet and Electromechanical Devices: Materials, Analysis, and Applications*, Academic Press, San Diego, CA, USA, 2001.

[34] W. Hu, Q. He, and B. Yang, "Design of a novel active joint mechanism for solar panels," in *Proceedings of the 2017 5th International Conference on Mechanical, Automotive and Materials Engineering (CMAME)*, pp. 174–177, Guangzhou, China, August 2017.

[35] W. Hu, Y. Gao, X. Sun, Y. Yang, and B. Yang, "Semi-active vibration control of a rotating flexible plate using stiffness and damping actively tunable joint," *Journal of Vibration and Control*, vol. 25, no. 21-22, pp. 2819–2833, 2019.

[36] J. Wei, D. Cao, L. Liu, and W. Huang, "Global mode method for dynamic modeling of a flexible-link flexible-joint manipulator with tip mass," *Applied Mathematical Modelling*, vol. 48, pp. 787–805, 2017.